PROCEEDINGS, 48th Workshop on Geothermal Reservoir Engineering
Stanford University, Stanford, California, February 6-8, 2023
SGP-TR-224

Elastic Characterization at Utah FORGE: P-wave Tomography and VSP Subsurface Imaging

Nori Nakata[13], Don W. Vasco[1], Peidong Shi[2], Tong Bai[3], Federica Lanza[2], Ben Dyer[4], Coral Chen[5], Sea-Eun Park[16], Hongrui Qiu[1]

[1]Earth and Environmental Sciences Area, Lawrence Berkeley National Laboratory, 1 Cyclotron Rd., Berkeley, CA 94720

[2]Swiss Seismological Service, ETH-Zürich, Zürich, Switzerland

[3]Earth, Atmospheric, and Planetary Sciences, Massachusetts Institute of Technology, 77 Massachusetts Ave, Cambridge, MA 02472

[4]Geo-Energie Suisse, Switzerland

[5]University of California, Berkeley, CA

[6]Department of Environment and Energy, Jeonbuk National University, Republic of Korea

nnakata@lbl.gov

Keywords: Seismic Tomography, VSP survey, Machine Learning, Utah FORGE

ABSTRACT

For understanding subsurface geology, fault locations, and fracture distribution, detailed subsurface structure information, such as velocity models and reflectivity images, is essential. The velocity models can be used for finding accurate earthquake locations and characterization. We use 3D seismic survey data collected in 2018 and a walkaway Vertical Seismic Profile (VSP) survey performed in 2022 to refine the elastic model at the FORGE EGS site, Utah.

We apply travel-time tomography for the 3D seismic survey, which contains nearly 1100 vibroseis shots and 1700 receivers. To increase the picking accuracy, we develop and test two approaches: a machine-learning-based (ML) picker and a frequency-dependent travel-time picker. For the ML picker, we combine the EQTransformer algorithm with cross-correlation to pick P-wave travel times. Although the EQTransformer is designed for earthquake waveforms, it can still pick accurate travel-times of active-seismic data compared to other ML pickers. The frequency-dependent picker is a new approach applied to the waveforms before correlating the vibroseis sweeps. In the waveforms, the sweep signals are recorded as linear upsweep signals. We use a time-frequency analysis to find the linear trend, which corresponds to the arrival time of the wave. Both methods match reasonably well with some differences, which will be discussed. Then we apply a tomographic inversion with the Eikonal solver to estimate the subsurface velocities with higher resolution than the model developed for migration.

The VSP survey was recorded after the 2022 April stimulation. The survey contains 106 vibroseis shot points, two DAS systems in nearby boreholes (78-32A and 78-32B), and two geophone systems (58-32 and 78-32B). Direct P and S waves are clearly observed with some reflections. Geophones generally have a higher signal-to-noise ratio than DAS, although DAS has much better spatial sampling. We apply reflection imaging using reverse-time migration, which reveals several reflectors that are imaged by previous studies, but we find the necessity of updating the velocity model for migration because of poor focusing.

1. INTRODUCTION

Subsurface elastic velocity models are the foundation of understanding subsurface geology, faults and fractures, and stress and strain states. In addition, elastic velocity models are often used for accurately locating earthquakes, as well simulating ground-motion due to earthquakes. Surface and borehole seismic surveys, as well as borehole logging data, have been widely employed for developing velocity models (Yilmaz, 2001). Here, we take advantage of recently observed seismic data at Utah FORGE EGS Site to develop an updated elastic model.

FORGE is a test facility in Utah that is hosting several deep geothermal stimulations (Moore et al., 2019). The stimulations are closely monitored using an array of geophysical, geochemical, and hydrological tools. These include seismic arrays and geodetic methods that are situated at or near the Earth's surface. In order to analyze these data it is necessary to have a reasonably good model of the elastic velocities from the surface downward to the injection locations. While there are models of shear wave velocity at the site, obtained by the analysis of surface waves (Zhang and Pankow, 2021), there are limited constraints on the compressional wave velocity. For example, most available well logs do not sample above a depth of 500 m, as indicated in Figure 1. Thus, the near-surface elastic properties of the site are not well characterized. This can be an impediment in the analysis of surface-based observations given that the velocity variations in the shallow regions can be quite significant.

We use two seismic datasets: 3D seismic data collected in 2018 and Vertical Seismic Profile (VSP) data collected in 2022. We first test two types of travel-time picking algorithms for the 3D seismic data to accurately measure P (and S) wave arrival times. Then we apply eikonal tomography to invert P-wave velocities down to around 1 km depth. Next, we apply wavefield migration to the VSP survey. Although the image is preliminary, we obtain several reflectors potentially related to the geologic layers.

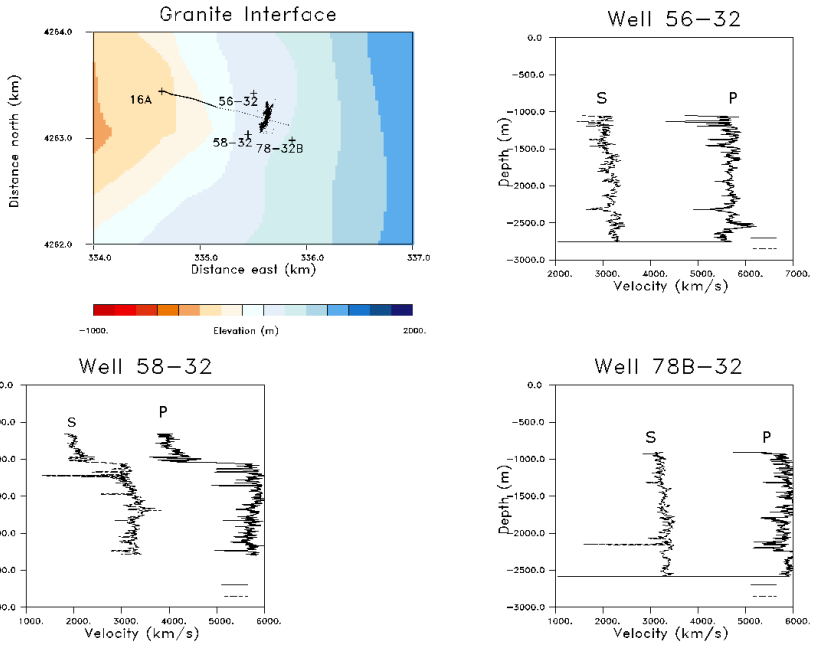

Figure 1. Elevation above mean sea level of the granite interface at the FORGE geothermal test site. Three observation wells (58-32, 56-32, and 78B-32) are labeled, as is the stimulation well (16A). The distribution of points denotes the cloud of seismicity associated with the stimulation. Available well-log data of seismic velocities are shown in each panel.

2. TRAVEL-TIME PICKING

Available observations from a reflection survey in 2018 (Figure 2) are sensitive to the shallow elastic properties at the FORGE site because of their source-receiver geometries. The primary motivation for the survey was to image the sediment-granite interface in the area, a major structural interface that is critical for drilling wells and designing an effective stimulation.

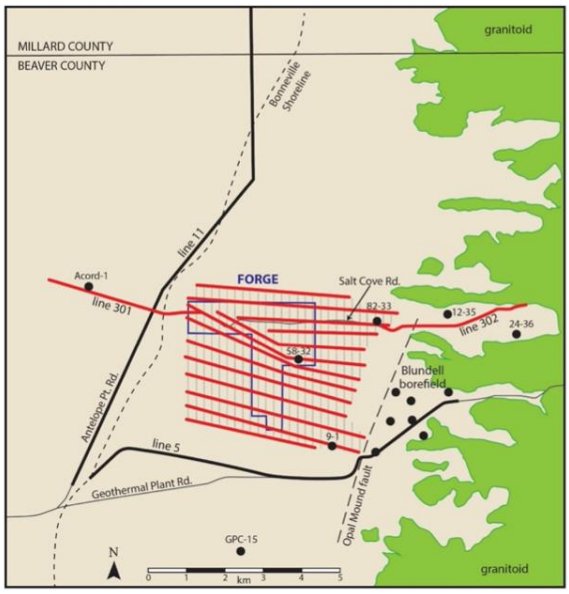

Figure 2. Geometry of the reflection survey used to image the structure beneath the FORGE geothermal test site. Red lines show the location of sources and black vertical lines are the locations of receivers.

However, the direct arrivals in the recorded seismic waveforms also contain important information on the shallow elastic properties. There are 1114 source positions and 1769 possible receivers with the potential for almost 2 million arrival times. The traces display clear direct

arrivals as well as reflections from the sediment-granite interface (Figure 3). One impediment to the use of the reflection waveforms is the sheer amount of work required to pick first arrivals for such a large volume of data. Therefore, we adopted two automated approaches for determining seismic arrival times. The first is a machine-learning (ML) approach that was developed for picking first arrivals from regional earthquakes. The second is a novel method that makes use of the vibro-seis frequency sweep and the separation of the signal from the micro-seismic background noise at frequencies above approximately 15 Hz.

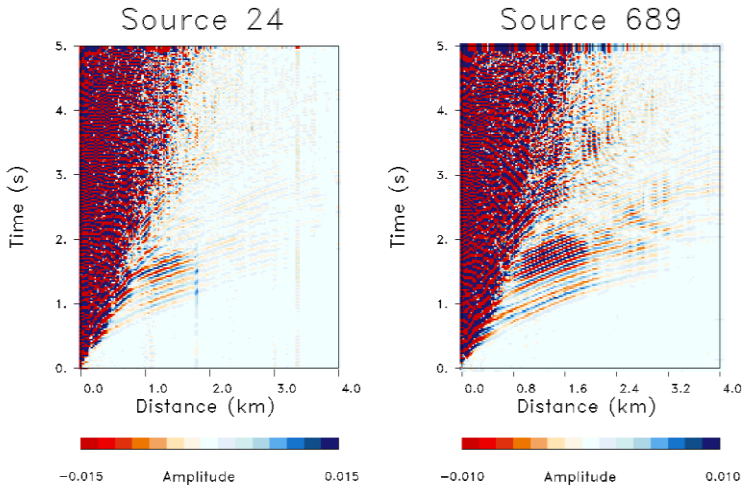

Figure 3. Seismic traces for two sources in the reflection surveys, shots 24 and 689. The traces are plotted as a function of distance from the shot.

2.1 Machine-learning-based travel-time picking

The 3D reflection seismic survey in the FORGE area acquired millions of seismic traces. Therefore, automatic and efficient methods are required to process this large data set. Encouraged by the superior performance of ML-based methods in picking seismic phases (Zhu and Beroza, 2018), we evaluate and apply ML techniques to pick the arrival times of the first breaks in the reflection seismic data set. Because no manual picks are available to build ground-truth labels and train dedicated ML models, we leverage existing ML models that are pre-trained using global natural earthquakes to perform this picking task. The tested pre-trained ML models are trained on local and regional earthquake data sets for picking the P- and S-phases of earthquakes (Woollam et al., 2022). As most natural earthquake data sets are collected at 50 to 200 Hz sampling rates, these pre-trained ML models are trained and expected to work at a fixed sampling rate of 100 Hz, requiring a particular time duration for the input segments, e.g. 30 seconds (Woollam et al., 2022). In comparison, the reflection seismic traces at FORGE are recorded at a 1000 Hz sampling rate and in a 4-seconds duration. Therefore, there is a systematic scale difference between the models' applicable range and the applied data set. To accommodate the scale difference, we vary the data sampling rate of the recorded reflection seismic data to permit the successful application of ML models and mimic the scale range of the typical earthquake waveforms. After different tests, we find that changing the data sampling rate to 60 Hz best fits our data set and permits a good performance of ML models for picking the first arrivals.

To build an automatic ML-based picking workflow, we employ SeisBench (Woollam et al., 2022), an integrated seismological ML model platform, to provide available ML models. SeisBench integrates various ML architectures (e.g. U-Net, CNN and Transformer) trained on different data sets (e.g. STEAD, GEOFON and SCEDC). We evaluate the performance of different ML models for picking the first wave arrivals of the FORGE data set and determine the best-fit model. We found that the best fit model is the EQTransformer model trained on the GEOFON data set as shown in Figure 4. After applying the best-fit model to all traces and with a picking threshold of 0.2, we obtain the first arrival times of the whole data set.

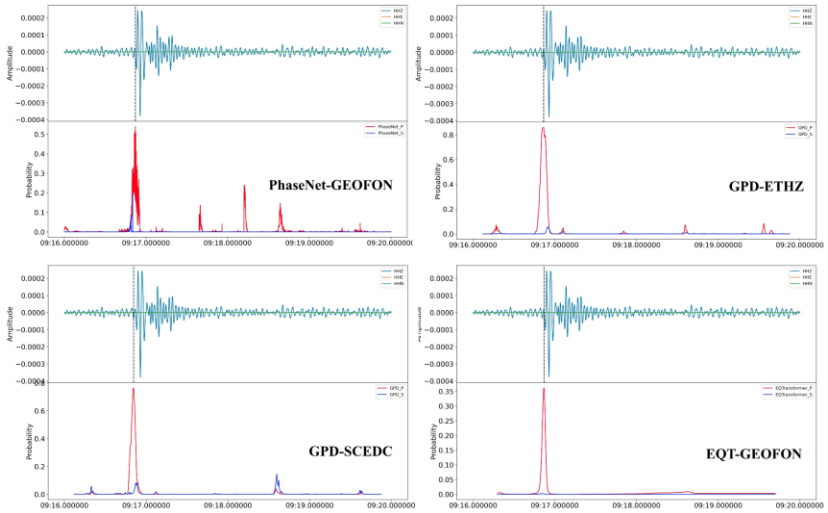

Figure 4. ML model performance comparisons for picking the first arrivals. The figure highlights four models with the model names indicated in each panel. For each panel/model, the upper frame shows the recorded seismic trace and the picked first arrival time, whereas the bottom frame shows the picking probabilities generated by the used ML model. In comparison, the EQT-GEOFON model performs the best.

Because the adopted ML model is designed and trained for picking arrival times of natural earthquakes, model generalization issues exist when applying the chosen ML model to the FORGE reflection seismic data. In addition, signal-to-noise ratio and non-direct phase arrivals with large amplitudes (e.g. surface waves and reflection waves) will affect the model's performance and cause false and incorrect picking results. As the source and receiver locations are known a priori, we calculate the theoretical arrival times of direct waves (e.g. first P arrivals) from a preliminary layered velocity model by solving eikonal equations. The theoretical arrival times with a specific tolerance range are then used as references to constrain the ML picking results. ML picks falling out of the theoretical arrival time tolerance range are removed. By incorporating theoretical arrival time constraints, we utilize spatial coherence of arrival times in the nearby traces and further eliminate outliers due to low SNR or interference from strong surface/reflection waves (Figure 5).

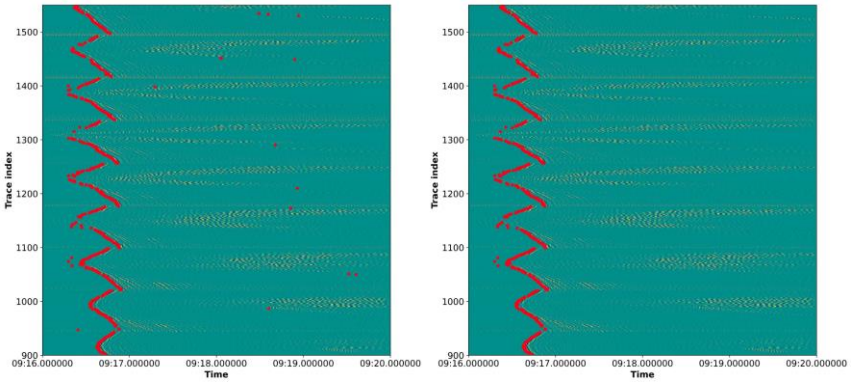

Figure 5. The left panel shows the original ML picking results for the first arrivals of a seismic profile (vertical axis for trace index and horizontal axis for recording time). The right panel shows the ML picking results after implementing theoretical arrival time constraints. The red dots in the figure highlight the picked arrival times. Note that the picking outliers which are induced by strong surface waves have been eliminated.

We notice that the ML picking performance is subject to SNR and sometimes shows picking uncertainties of several milliseconds for traces with low SNR. To further improve the picking accuracy, we use cross-correlation to fine-tune the obtained picks. For each shot gather, we stack the waveforms of high-quality picks (with ML probabilities higher than 0.5) to generate a standard wavelet of the direct arrivals (Figure 6a). Each picked trace in this shot gather is then cross-correlated with the standard wavelet to resolve the time lag (Figure 6c) and shift accordingly to obtain a more precise picking result (Figure7). We notice that most picked traces (90%) have a lag time within 10 milliseconds (Figure 6c) and a correlation coefficient larger than 0.6 (Figure 6b), which demonstrates the reliability of most ML picks (Figure 7).

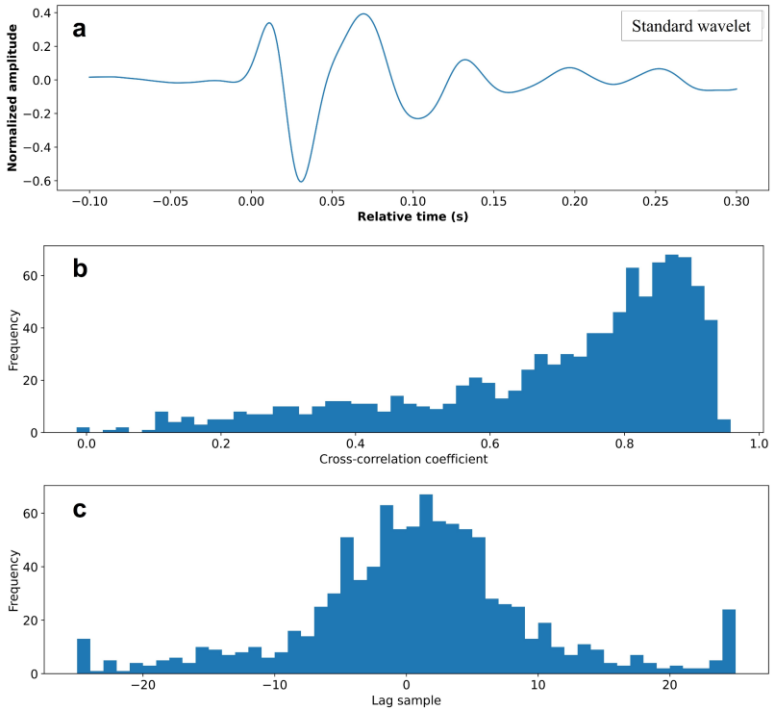

Figure 6. (a) Example of a stacked standard wavelet of the direct arrivals for a shot gather. The standard wavelet is obtained by stacking the waveforms from 0.1 seconds before and 0.3 seconds after the high-quality picks. (b) The maximum cross-correlation coefficients between the picked traces and the standard wavelet for the same shot gather of (a). (c) The lag time in samples between the picked traces and the standard wavelet when the cross-correlation coefficient reaches the maximum.

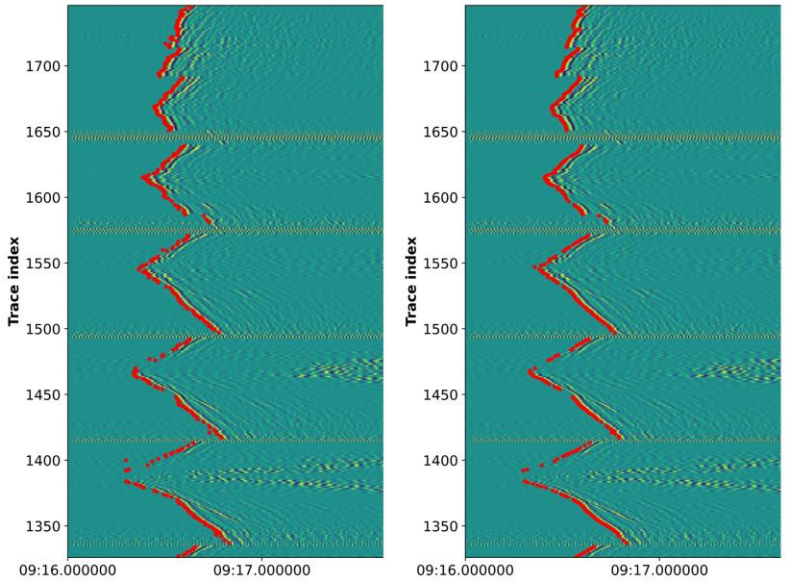

Figure 7. The picking results before (left) and after (right) applying the cross-correlation refinement.

Overall, the complete workflow consists of three parts: (1) ML-based first arrivals picking, (2) theoretical arrival time constraint, and (3) cross-correlation refinement. With this automatic workflow that combines ML-picking and cross-correlation refinement(Figure 8), we demonstrated that we can efficiently pick the first arrivals, which, in turn, can be readily used in tomography studies.

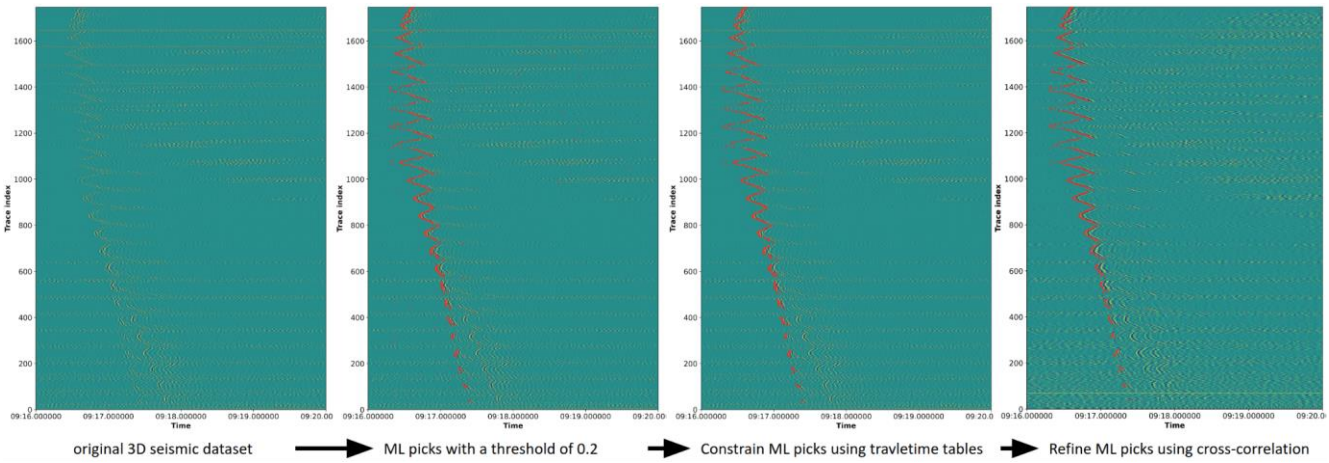

Figure 8. Automatic first-arrival picking workflow using ML and cross-correlation techniques (Step 1 through 3 in the text).

2.2 Travel-time estimation from the frequency sweep

The vibro-seis source used for the FORGE reflection survey has a clear linear increase in frequency as a function of time, visible in both the recorded trace and in a time-frequency decomposition of the trace (Figure 9). This trace is sufficiently close that the non-linear ground motion and the clipping of the signal amplitude are visible in both the raw trace and in the time-frequency decomposition. In the time-frequency plot the non-linearity introduces frequency multiples that appear as lines with steeper slopes in the lower panel of Figure 9. The non-linear ground motion decreases rapidly with distance from the source and, at a sufficiently large distance, only the primary sweep is visible (Figure 10). An interesting feature visible in the time-frequency decomposition in Figure 10 is the separation between the background micro-seismic noise and the vibro-seis signal that occurs at frequencies above about 10-15 Hz. This separation between signal and noise is visible in traces that are over 5 km from the source.

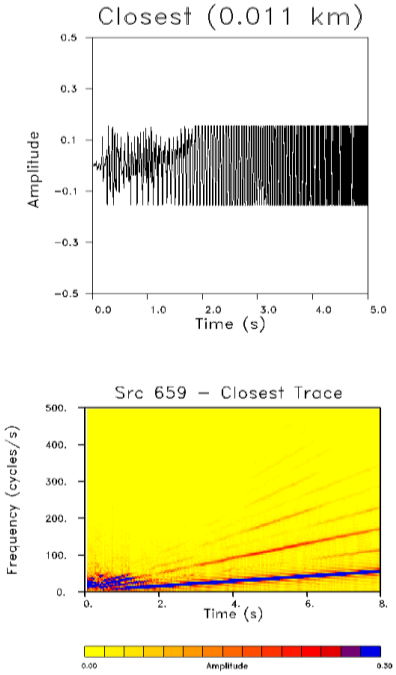

Figure 9. (Upper panel) Seismic trace recorded 11 m from the vibro-seis source. (Lower panel) Time-frequency decomposition of the seismic trace shown in the upper panel.

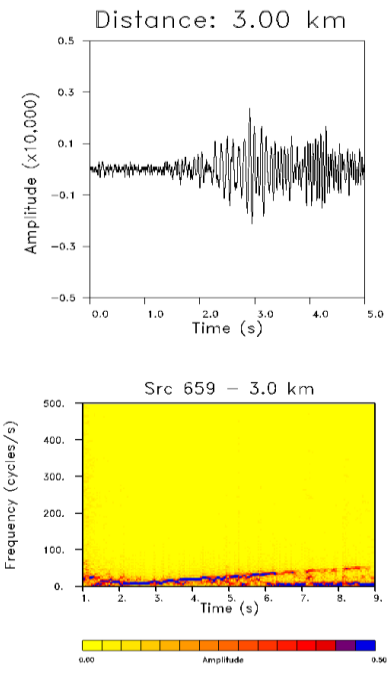

Figure 10. (Upper panel) Seismic trace recorded 3 km from the vibro-seis source. (Lower panel) Time-frequency decomposition of the seismic trace shown in the upper panel.

The appearance of the linear sweep at a seismic station provides information on the arrival time of a propagating waveform from the source. One idea for automating the estimation of travel times from the seismic waveforms gathered during the reflection survey is to make use of the detection of the linear sweep at a station. Our first approach was to adopt a robust line fitting algorithm in order to define an 'arrival' for a particular frequency. The slopes of the lines in time-frequency space appear to be constant at the stations, indicating that attenuation was not strong and that the propagation is non-dispersive. Thus, we fixed the slope of the fit lines and just altered the intercept, for a single fitting parameter for each trace. This approach seemed reliable and the results agreed reasonably well with the machine-learning picks and estimates from eikonal equation calculations. However, another method, based upon slant-stacking amplitudes along lines with the same slope but varying intercepts, seemed simpler and perhaps more robust for noisy data. As an example, consider the receiver that is the furthest from source 24, over 5 km away from the shot. The raw trace for this source-receiver pair is very noisy and even the machine-learning picking algorithm failed to pick an arrival from the correlated vibro-seis data. The linear time-frequency sweep of the vibro-seis is clearly seen in the time-frequency decomposition, along with a constant 60 Hz component due to electrical noise. In the slant-stacking method we sum the squared amplitudes along lines with the same slope as given by the vibro-seis source-time function. The resulting root-mean-squared amplitude as a function of the line offset is shown in Figure 11. There is a clear peak in the summation slightly before 1.0 second. The slant-stack approach is easy to implement as a computer code and is simple to parallelize. The non-parallel version runs on a work station and only takes a fraction of a second to estimate an arrival. Still, for all 1.4 million traces it took about a week of computing, which was done in the background. The estimated travel times are shown in map view in Figure 12 for sources 116 and 538. Note how the arrival times are earlier for stations to the east where the granite is shallow due to its much higher velocity (see Figure 1). An initial velocity model was constructed from information that was available from both the well logs and from the reflection survey information, prior to a full tomographic inversion of all travel times. Below the granite interface that was defined by the reflection survey, the compressional velocity was assumed to be a constant 5.84 km/s, as indicated by the well logs in Figure 1. Above the dipping sediment-granite interface, the compressional wave speeds from the velocity analysis used to reduce the reflection data was used for the sediments.

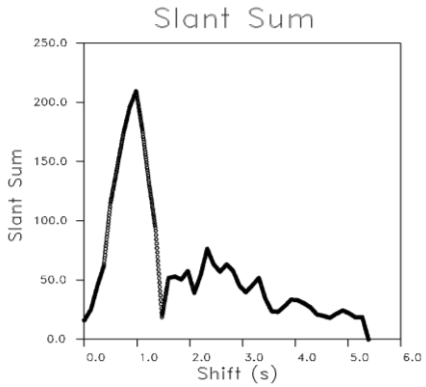

Figure 11. Result of the summation of the amplitudes along dipping lines in time-frequency space plotted as a function of the lateral shift of the line.

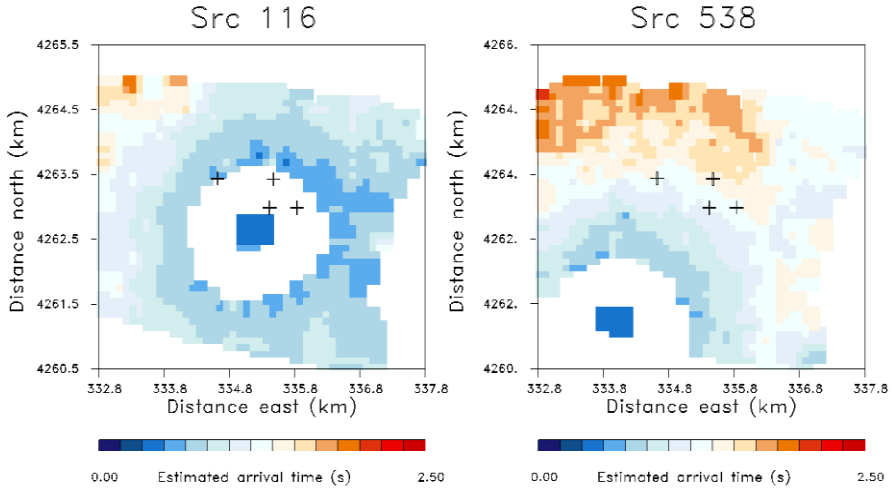

Figure 12. Map views of the arrival times for two sources (116 and 538) from the reflection survey. The crosses denote the three wells labeled in Figure 1 and the well head of the stimulation well (16A) that lies to the west of the trio of wells.

3. P-WAVE TOMOGRAPHY

Here, we use travel times estimated by the time-frequency analysis for tomography, and will incorporate the ML pickers in the future. A finite-difference eikonal equation solver was used to calculate the travel times through the hybrid velocity model and to define the rays that are used in the tomographic inversion. Comparisons between the estimated travel times and the eikonal travel times indicate general agreement between the observed and calculated times. In Figure 13, we plot the observed and calculated travel times as functions of distance from source for the two shots considered in Figure 12. There is a general agreement between the two sets of travel times, though there is much more scatter in the observed ones than in the calculated ones. Note that, for far offsets, the travel times separate into fast and slow branches, likely due to the granite that is encountered along some azimuths while sediments are found for paths in other directions. This branching at farther offsets is seen in both the observed and calculated travel times.

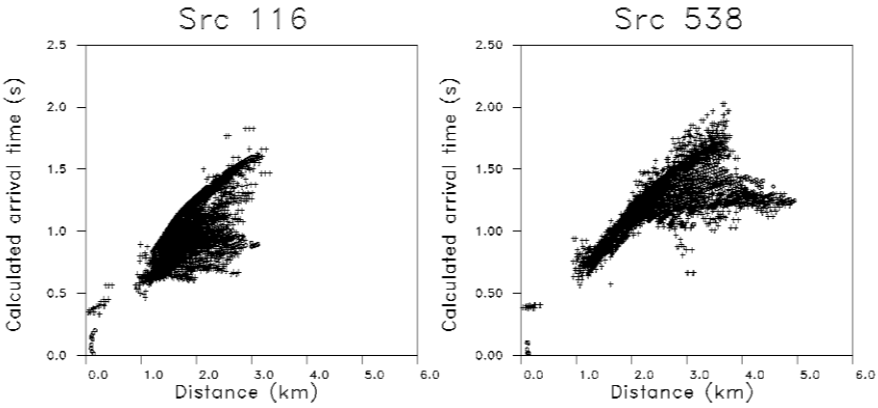

Figure 13. Arrival times as functions of source-receiver separation. The open circles denote the times calculated using the initial velocity model and an eikonal solver. The plus signs denote the travel times estimated using the slant-stack approach.

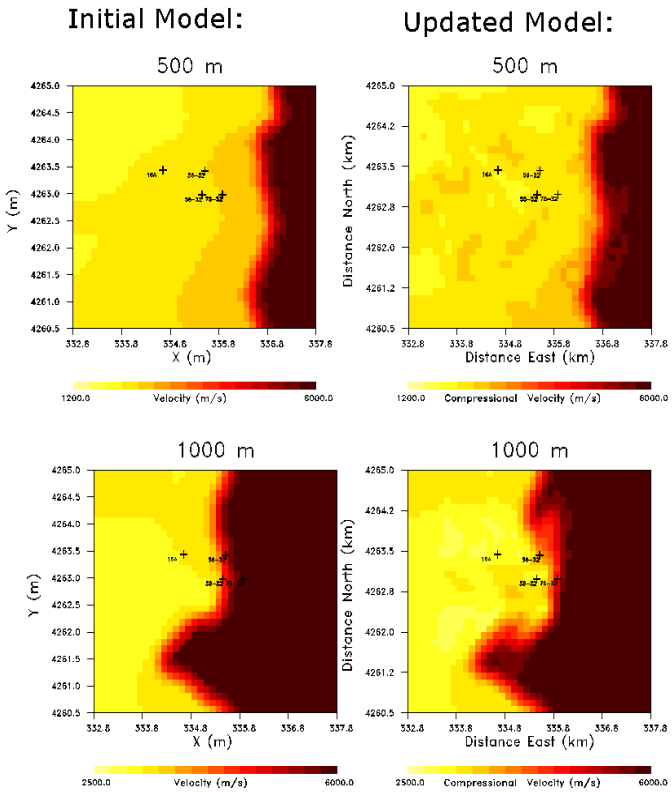

Figure 14. Horizontal slice through the velocity model at depths of 500 m and 1000 m. The left panels show the initial model and the updated model is shown on the right.

Using the initial model as a starting point, we performed a tomographic inversion of the roughly 1.4 million arrival times. The least squares QR algorithm (LSQR) was used for the sparse matrix inversion. The sensitivities were based upon ray-paths that were back-calculated

from the eikonal solver travel time fields for each source. That is, by starting at each receiver and traveling down the gradient of the travel time field until the source was reached. We show the results of a linearized inversion, as we did not iteratively update the model beyond the first update. Both source and receiver travel time shifts were included in the inversion to account for residual statics and shallow velocity anomalies as well as potential station mis-locations. The resulting updated velocity model is shown in Figures 14 and 15.

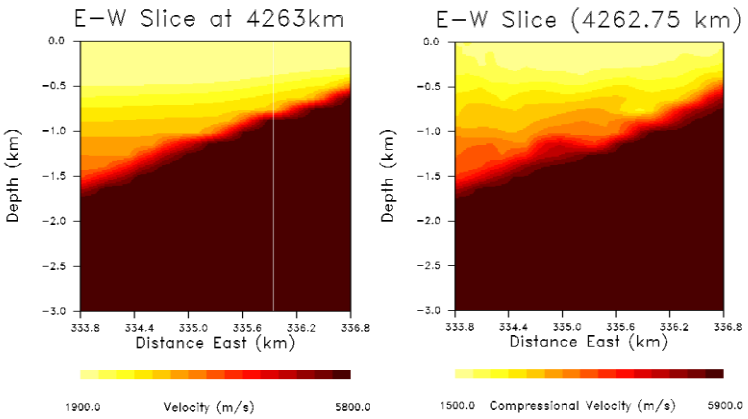

Figure 15. Vertical slice through the velocity model for a plane that lies along the EW axis. The left panel shows the initial model and the model update is shown on the right.

4. VERTICAL SEISMIC PROFILING

For the VSP survey, 106 vibroseis shots are excited at spacing of 30 m, approximately along a 2D line in SE-NW direction (Figure 16). Two DAS arrays with 1010 and 1260 active channels are placed in wells 78A-32 (green dots in Fig. 16) and 78B-32 (red dots in Fig. 16), respectively. Two three-component 8-level geophone chains (orange and black inverted triangles in Fig. 16) are placed at the depth of ~1600-2000 m in wells 58-32 and 78B-32, respectively. Figure 17 displays receiver gathers at one three-component geophone in 78B-32. Note the strong conversion waves observed in the N- and E-components. Sample DAS data at well 78A-32 and 78B-32 are shown in Figure 18. Figure 19 compares the waveforms recorded by DAS and geophones.

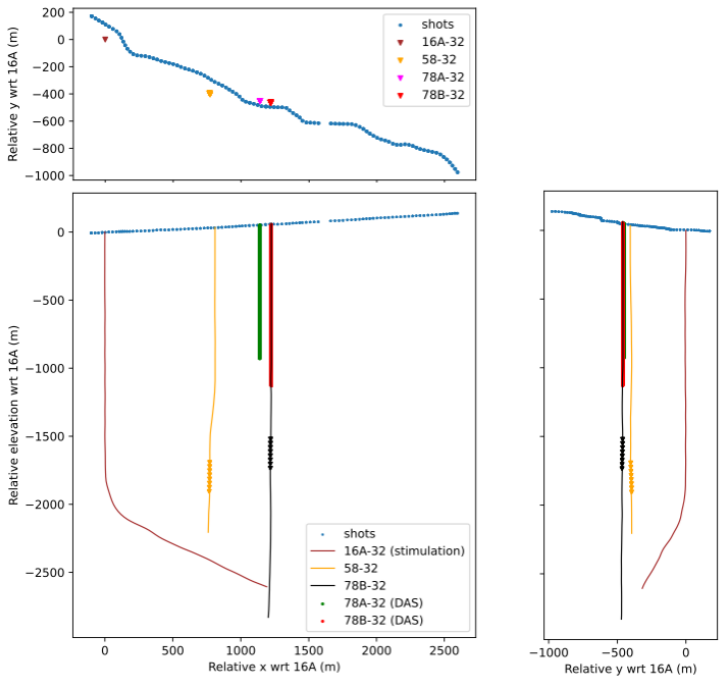

Figure 16. VSP Survey acquisition geometry. The vibroseis shots are represented by blue dots. The brown, orange and black lines denote the trajectories of well 16A-32 (stimulation well), 58-32 and 78B-32, respectively.

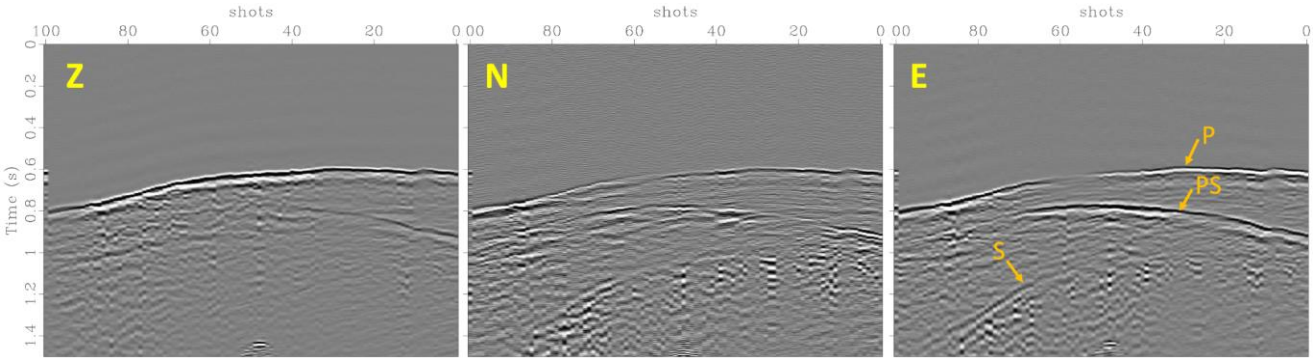

Figure 17. The three-component receiver gather at the deepest geophone (black triangle) in well 78B-32.

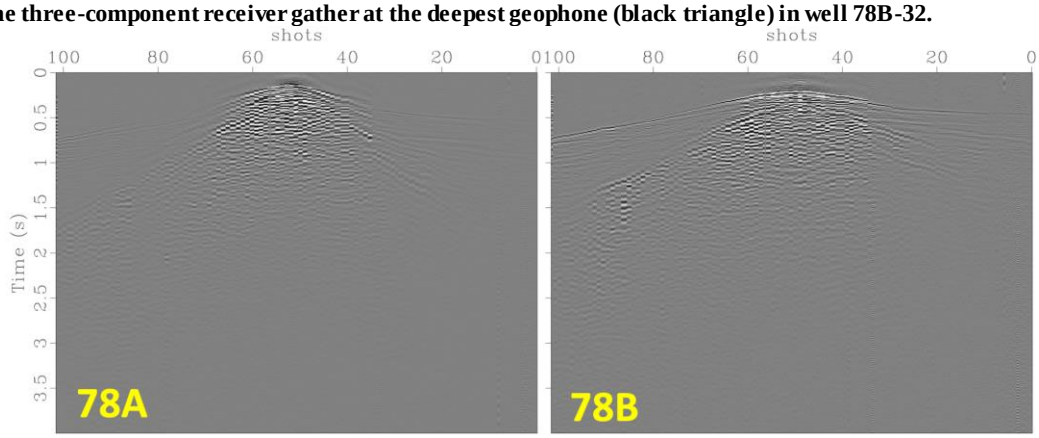

Figure 18. Receiver gathers at one DAS channel at depth of 700 m in well 78A-32 and 78B-32, respectively.

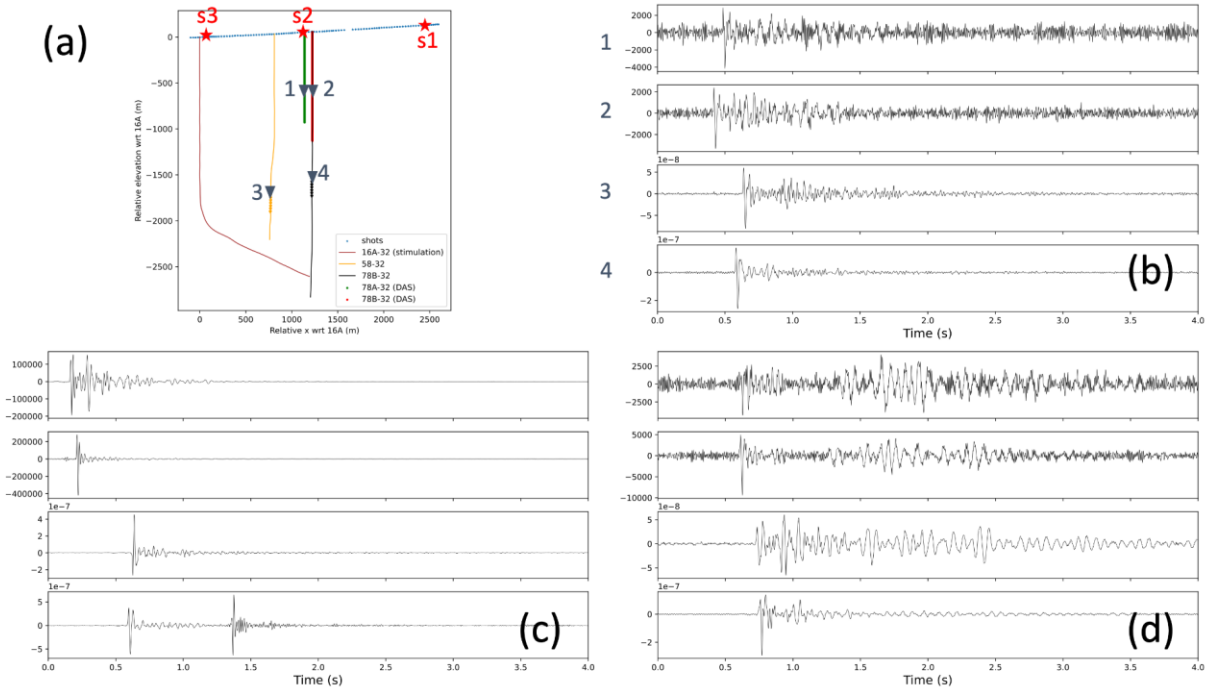

Figure 19. Waveform comparison of DAS channels (1 and 2) and Z-component of two geophones (3 and 4), corresponding to the three vibroseis sources: (b) s1, (c) s2, and (d) s3.

We extract the P-wave RMS velocity along the 2D profile from the 3-D seismic reflection survey, and conduct the dix- and time-to-depth conversion, to obtain the 2D-Vp profile for imaging (Figure 20). We then choose the DAS data from well 78A-32 to image the subsurface structure. We extract the up-going components in the F-K domain (Figure 21), and apply the reverse-time migration (RTM) algorithm as follows: (1) we inject the time-reversed obtained data at corresponding DAS channels to obtain the receiver wavefield; (2) we simulate the source-side wavefield with 60-Hz (the dominant frequency of the observed data) Ricker wavelet; (3) we apply zero-lag cross-correlation of the source- and (time-reversed) receiver- wavefield for a single-shot RTM image; and finally (4) obtain the stacked RTM images from multiple shots.

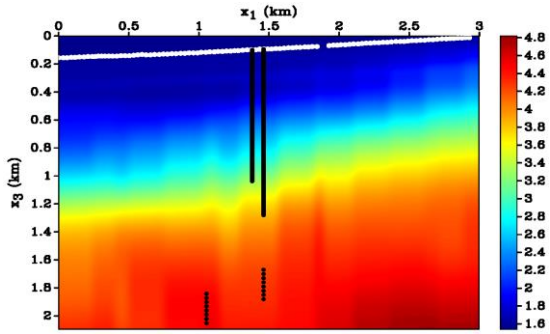

Figure 20. Vp model along the 2D line. The DAS channels and geophones are denoted by black dots, and the vibroseis shots by white dots.

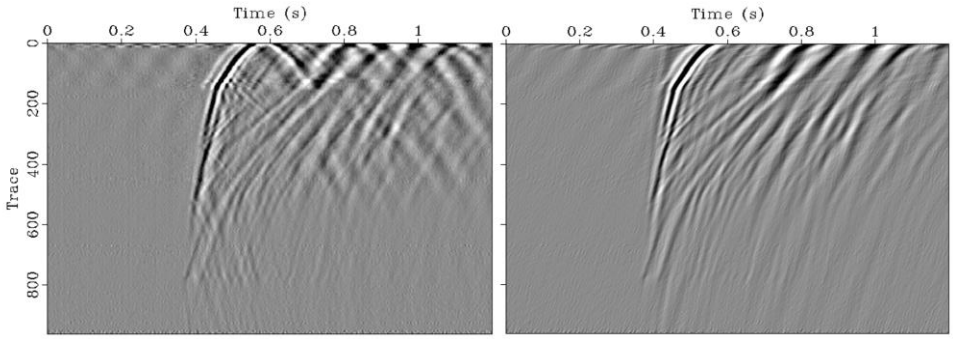

Figure 21. A sample shot gather recorded at DAS channels in well 78A-32. Left: original data; right: decomposed up-going waves.

Some sample single-shot RTM images and corresponding shot gathers are shown in Figure 22, with relatively strong upgoing reflections marked by colored arrows. The stacked RTM image (Figure 23a) is contaminated by strong artifacts particularly around the well, which is caused by the complex wavefield at these shot locations (see Figure 18). To clean the results, we clip each single-shot image outside the shot-receiver range. Moreover, we only select shots with strong reflections (such as those in Figure 22) and apply selective stacking. The final RTM image (Figure 23b) is much cleaner, with main reflectors marked by the dotted lines.

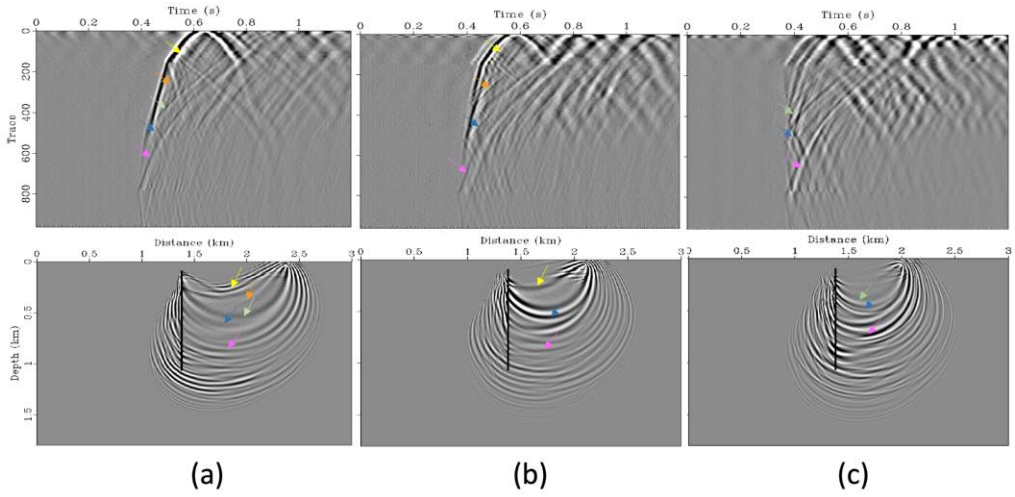

Figure 22 Sample shot gathers (upper panels) and corresponding RTM images (lower panels) at shot (a) #7, (b) #10, and (c) #12. Obvious upgoing waves and the corresponding reflections are marked by colored arrows.

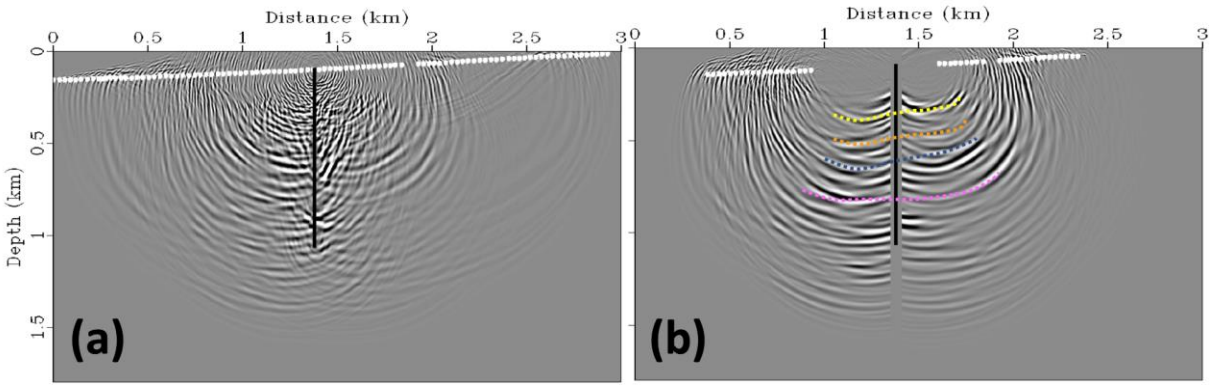

Figure 23 RTM images using (a) all shots, and (b) selected shots with acquisition artifacts removed. The black line marks the DAS channels at well 78A-32, and white dots denote corresponding shot locations.

5. CONCLUSIONS

We use surface and borehole seismic data to develop an elastic velocity model at the Utah FORGE EGS site. The travel times between source-receiver pairs are needed for travel-time tomography, but accurately estimating them from the waveforms is nontrivial and time consuming. We propose to use two different methods for the travel-time picking using machine learning and time-frequency analysis. Both provide reasonable results according to the visual inspection with waveforms. We will compare the picks from both methods to estimate more robust travel times. Because of the dense networks of sources and receivers, we have 1.4 million travel times and use them for tomography. The tomography is based on the eikonal solutions of travel times. The updated velocity model follows the general trend of the geologic model, e.g., dipping towards west, but it shows a more detailed structure.

We also use a walkaway VSP data recorded in April 2022. Interestingly, the shot data are recorded by both DAS and geophones. Geophones generally show a better signal-to-noise ratio, but the densely sampled waveforms recorded by DAS are also beneficial for imaging. We apply reverse-time migration to the observed DAS data in well 78A-32. Although the RTM image is contaminated by migration artifacts, it shows several significant interfaces potentially related to the geological layers. The dip of the layers corresponds to the general dip (of what?) in the region. We will apply travel-time tomography to this VSP data to jointly estimate better velocity models at the Utah FORGE, and then use them for imaging.

6. ACKNOWLEDGMENTS

We are grateful to the Utah FORGE project for providing seismic and borehole datasets and collaboration. The data are available through the Geothermal Data Repository. This work is supported by the De-Risking Enhanced Geothermal Energy project (Innovation for DEEPs). DEEP is subsidized through the Cofund GEOTHERMICA, which is supported by the European Union's HORIZON 2020 programme for research, technological development, and demonstration under Grant Agreement Number 731117.

REFERENCES

Moore, J., McLenna, J, Allis, R., Pankow, K., Simmons, S. Podgorney, R., Wannamaker, P., Bartley, J., Jones, C., and Rickard, W. (2019) The Utah Frontier Observatory for Research in Geothermal Energy (FORGE): An International Laboratory for Enhanced Geothermal System Technology Development, 44th Workshop on Geothermal Reservoir Engineering, SGP-TR-214.

Woollam, J., Münchmeyer, J., Tilmann, F., Rietbrock, A., Lange, D., Bornstein, T., Diehl, T., Giunchi, C., Haslinger, F., Jozinović, D., Michelini, A., Saul, J., & Soto, H. (2022). SeisBench—A Toolbox for Machine Learning in Seismology. Seismological Research Letters, 93(3), 1695–1709. https://doi.org/10.1785/0220210324

Yilmaz, Ö. (2001), Seismic Data Analysis, Society of Exploration Geophysicists

Zhang, H., & L. Pankow, K. (2021). High-resolution Bayesian spatial autocorrelation (SPAC) quasi-3-D Vs model of Utah FORGE site with a dense geophone array. Geophys. J. Int., 225(3), 1605–1615.

Zhu, W., & Beroza, G. C. (2018). PhaseNet: A Deep-Neural-Network-Based Seismic Arrival Time Picking Method. Geophysical Journal International, 216(1), 261–273. https://doi.org/10.1093/gji/ggy423